Electronic states and magnetotransport in unipolar and bipolar graphene ribbons

Alessandro Cresti,[1,2] Giuseppe Grosso,[1] and Giuseppe Pastori Parravicini[3]
[1]*NEST-CNR-INFM and Dipartimento di Fisica "E. Fermi," Università di Pisa, Largo Pontecorvo 3, I-56127 Pisa, Italy*
[2]*NEST-CNR-INFM and Scuola Normale Superiore, Piazza dei Cavalieri 7, I-56126 Pisa, Italy*
[3]*NEST-CNR-INFM and Dipartimento di Fisica "A. Volta," Università di Pavia, Via A. Bassi 6, I-27100 Pavia, Italy*
(Received 21 December 2007; published 6 March 2008)

The electronic structure and the current profiles of *n*- and *p*-doped graphene ribbons are investigated within the Keldysh–Green's function method in the tight-binding framework. The low energy spectrum, at the heart of the relativisticlike quantum transport, is studied numerically and relevant features are understood analytically by means of the continued fraction tool. Simulations of charge transport and spatial distribution of spectral currents in field-effect controlled graphene ribbons are then carried out in the absence and in the presence of uniform magnetic fields. The role of gated regions and threading magnetic fields for manipulating the flow of Dirac particles is investigated.

DOI: 10.1103/PhysRevB.77.115408 PACS number(s): 73.63.Bd, 73.23.−b

I. INTRODUCTION

Graphite and layered compounds have always attracted a wide interest because of the peculiar effects of structural anisotropy on their electronic, magnetic, vibrational, and optical properties. Early and recent investigations[1–8] concerning the electronic states and physical properties of graphite and other isoelectronic or isostructural anisotropic materials have highlighted the key role of the geometrical bipartite honeycomb lattice, and the Dirac-like structure of the low energy quasi particles in the strictly two-dimensional hexagonal carbon lattice.[9]

Only recently, monolayers of carbon atoms (graphene) have been obtained under controlled protocols,[10–12] and an explosion of interest has accompanied this experimental breakthrough. Soon after, graphene monolayers and bilayers have entered the arena of new materials with the highest interest from a fundamental and technological point of view.[10–13] Carrier density in graphene can be controlled electrostatically and varied from unipolar to bipolar character with external local gates; *p*-type and *n*-type materials, planar *n*-*p* junctions, and other multiple junction devices have been fabricated[14–17] with appropriate field-effect geometries, thus opening novel architectures along the applicative road of carbon-based materials.

Among the unconventional transport properties of graphene due to the peculiar conical shape of the energy bands at the corners of the Brillouin zone, we mention the half-integer relativistic Hall effect,[11–13] the minimum conductivity of graphene ribbons,[18–23] the role of localized and extended impurities,[20,21] the diffusivelike shot noise[22,23] in gated samples, the easy tunneling of relativistic carriers through high and long barriers[24,25] (Klein tunneling), and the realization of superlenses by focusing of electron beams.[26,27] In this paper, we also show that the spatial distribution of spectral currents exhibits peculiar aspects, which are related to the charge conjugation symmetry of the Dirac equation. The theoretical and numerical procedures for imaging microscopic currents, based on the nonequilibrium Keldysh formalism[28–30] and the tight-binding framework along the guidelines of previous works,[31,32] emerge as an invaluable tool also for understanding or designing carbon-based devices.

In Sec. II, we give a brief description of the electronic structure of graphene, within the tight-binding model and a minimal basis set of dangling orbitals. In Sec. III, we study the electron and hole states of graphene ribbons both numerically and analytically. Different from other treatments in the literature,[1–7] we consider an atomistic description of the electronic states based on tridiagonal matrices and continued fractions expansion. In particular, we obtain the energy levels at the Dirac points and the zero energy modes of graphene ribbons with zigzag edges analytically. In Sec. IV, the nonequilibrium Keldysh formalism, widely applied in the study of charge transport in conventional two-dimensional electron gases in square lattices,[31–36] is adapted to the honeycomb topology[23,37] to obtain maps of currents in graphene ribbons under applied external fields. The maps allow a pictorial description of electronic transport and magnetotransport. Furthermore, in the case of superimposed gates, they provide a real space view of the Klein tunneling currents and suggest the way to realize manipulation of currents. Section V contains the conclusions.

II. ELECTRONIC STATES AND LANDAU LEVELS IN GRAPHENE

In this section, we briefly consider a few aspects of the electronic structure of graphene useful for a better self-contained presentation of the transport properties. The monolayer crystal structure of graphene is described by the typical honeycomb lattice with two carbon atoms in the primitive cell. The primitive translation vectors $(\mathbf{t}_1,\mathbf{t}_2)$ of the two-dimensional hexagonal lattice and the positions $(\mathbf{d}_1,\mathbf{d}_2)$ of the two atoms in the primitive cell are indicated in Fig. 1(a); the lattice constant is $a=2.46$ Å. The corresponding hexagonal Brillouin zone is indicated in Fig. 1(b).

The valence bands and the lowest energy conduction bands of graphene are mainly originated by the $2s$ and $2p$ orbitals of the carbon atoms. In the honeycomb lattice, there are two carbon atoms per primitive cell; this entails a minimal basis of eight Bloch sums. The six Bloch sums, formed

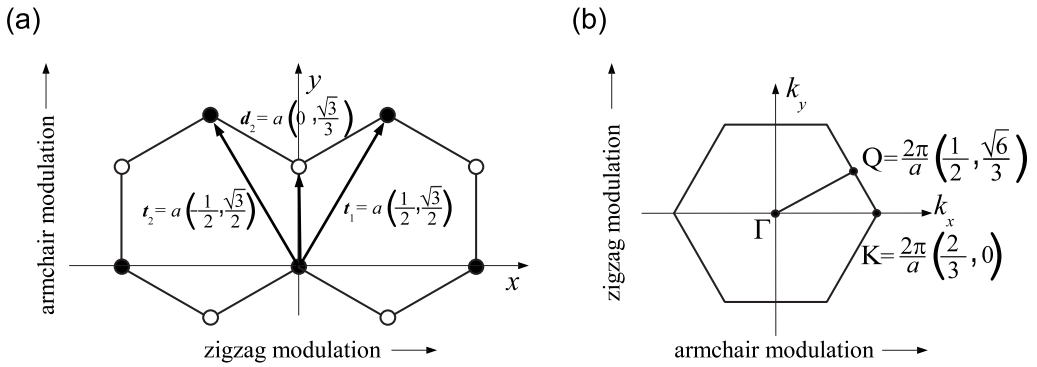

FIG. 1. (a) Lattice structure of graphene with zigzag modulation along the x direction and armchair modulation along the y direction. (b) Corresponding two-dimensional Brillouin zone.

with the s, p_x, and p_y orbitals, give rise to the σ bands; the sp^2 orbital hybridization guarantees the mechanical stability of the sheet and generate the valence bands. The three antibonding combinations of s, p, and p_y generate unoccupied conduction bands. Similarly, the two Bloch sums, based on the p_z orbitals of the two carbon atoms in the primitive cell, give rise to the π (valence) and π^* (conduction) bands. The group theory analysis of the honeycomb topology[1–4] shows that the π bands are degenerate at the corner points of the hexagonal Brillouin zone and have linear energy-wave-vector dispersion nearby (Dirac points). In undoped graphene, the Fermi energy occurs at the Dirac degenerate points.

Within the minimal basis set of two Bloch sums, formed by the p_z carbon orbitals of each sublattice, the crystal Hamiltonian is represented at each two-dimensional $\mathbf{k}$ vector, by the 2×2 semiempirical matrix,

$$H(\mathbf{k}) = \begin{pmatrix} 0 & tF(\mathbf{k}) \\ tF(\mathbf{k})^* & 0 \end{pmatrix}, \tag{1a}$$

where

$$F(\mathbf{k}) = 1 + 2\cos\frac{k_x a}{2}\exp\left(-i\frac{k_y b}{2}\right) \text{ and } b = a\sqrt{3} = 4.26 \text{ Å}. \tag{1b}$$

In the above equations, $F(\mathbf{k})$ denotes the geometrical structure factor of the honeycomb topology. The hopping parameter of the crystalline Hamiltonian between two nearest neighbor p_z orbitals is set to $t=-3$ eV, which provides a satisfactory description of the energy bands near the Dirac points in an orthogonal nearest neighbor tight-binding model.[5] The energy of the p_z orbitals is chosen as reference energy and set equal to zero. From Eqs. (1a) and (1b), the π and π^* energy bands are expressed as

$$E(\mathbf{k}) = \mp t|F(\mathbf{k})|. \tag{2}$$

The π valence band and the π^* conduction band are degenerate at the Dirac points $K=(2\pi/a)(2/3,0)$ and $K'=(2\pi/a)(-2/3,0)$, and at the other equivalent corner points of the Brillouin zone, where the structure factor vanishes.

Around the Dirac points the geometrical structure factor [Eq. (1b)] can be linearized in the wavevector components, and the Hamiltonian (1a) near K takes the simplified form,

$$H(\mathbf{k}\approx K) = \frac{\sqrt{3}}{2}\frac{1}{\hbar}a|t|\begin{pmatrix} 0 & \hbar k_x - i\hbar k_y \\ \hbar k_x + i\hbar k_y & 0 \end{pmatrix}, \tag{3}$$

where the wave vector $\mathbf{k}$ is defined with respect to the value of the wave vector at the degeneracy point. Similarly, $H(\mathbf{k}\approx K')$ is obtained replacing k_x with $-k_x$ in Eq. (3). The dispersion curves assume the typical conical shape,

$$E(\mathbf{k}) = \mp\frac{\sqrt{3}}{2}|t|ka \text{ with } k = \sqrt{k_x^2 + k_y^2}, \tag{4}$$

and the carriers near the degeneracy points behave as relativistic massless Dirac particles.

We consider now the effect of a uniform magnetic field, along the z direction, on the graphene energy spectrum around the Dirac points. Within the tight-binding model, we describe the magnetic field by means of the minimal substitution, which consists in replacing the components of the wave vector in the matrix elements of the Hamiltonian, with the generalized momentum operators,

$$\hbar\mathbf{k} \to \mathbf{p} + \frac{e}{c}\mathbf{A}(\mathbf{r}). \tag{5}$$

In the first Landau gauge $\mathbf{A}(\mathbf{r})=(-By,0)$, one obtains

$$\hbar k_x \to p_x - \frac{eB}{c}y \equiv \pi_x, \quad \hbar k_y \to p_y \equiv \pi_y, \quad [\pi_x,\pi_y] = i\frac{\hbar^2}{l_0^2}.$$

The magnetic length is $l_0=\sqrt{c\hbar/eB}\approx 257$ Å for $B=1$ T and $l_0\approx 80$ Å for $B=10$ T. The matrix Hamiltonian (3) becomes

$$H = \frac{\sqrt{3}}{2}\frac{1}{\hbar}a|t|\begin{pmatrix} 0 & \pi_x - i\pi_y \\ \pi_x + i\pi_y & 0 \end{pmatrix} = \gamma\begin{pmatrix} 0 & \eta^\dagger \\ \eta & 0 \end{pmatrix}$$
$$\text{with } \gamma = \frac{\sqrt{3}}{\sqrt{2}}\frac{a}{l_0}|t|, \tag{6}$$

where the annihilation operator η and the creation operator $\eta^\dagger$ are defined as

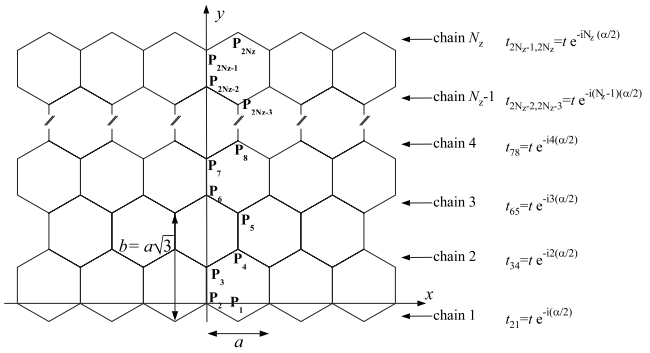

FIG. 2. Schematic representation of the lattice structure of a graphene ribbon with N_z longitudinal zigzag chains; the primitive cell and the $2N_z$ carbon atoms within the primitive cell are indicated. In the presence of a magnetic field, the hopping energies between nearest neighbor orbitals are modified by the Peierls phase factor as indicated in the right part of the figure.

$$\eta = \frac{l_0}{\hbar}\frac{1}{\sqrt{2}}(\pi_x + i\pi_y), \quad \eta^\dagger = \frac{l_0}{\hbar}\frac{1}{\sqrt{2}}(\pi_x - i\pi_y),$$

with $[\eta, \eta^\dagger]=1$. For $B=1$ T, for instance, we have $\gamma \approx 35$ meV, while $\gamma \approx 113$ meV for $B=10$ T. The diagonalization of the Hamiltonian (6) is trivial noticing that the squared matrix has diagonal form.[38] In fact,

$$H^2 = \gamma^2 \begin{pmatrix} 0 & \eta^\dagger \\ \eta & 0 \end{pmatrix}\begin{pmatrix} 0 & \eta^\dagger \\ \eta & 0 \end{pmatrix} = \gamma^2 \begin{pmatrix} \eta^\dagger\eta & 0 \\ 0 & \eta^\dagger\eta + 1 \end{pmatrix}. \quad (7)$$

The eigenvalues of the upper block and lower block of H^2 are thus $n\gamma^2$ with $n=0,1,2,\ldots$ and $(m+1)\gamma^2$ with $m=0,1,2,\ldots$. Thus, the eigenvalues of the Hamiltonian (6) are

$$E_n = \pm\gamma\sqrt{n}, \quad n=0,1,2,3,\ldots, \quad (8)$$

where all the eigenvalues are nondegenerate. A similar reasoning can be performed on the partner valley, and thus all magnetic bands are doubly degenerate. Such a spectrum is at the origin of the relativistic quantum Hall effect observed[11,12] in the conductance of graphene ribbons.

III. ELECTRONIC STRUCTURE OF GRAPHENE WIRES WITH ZIGZAG LONGITUDINAL MODULATION

In this section, we study the electronic structure of zigzag graphene ribbons of finite width W and arbitrary large length in the longitudinal x direction with analytic and numerical procedures. The lattice structure of graphene wires is depicted in Fig. 2. N_z is the number of zigzag longitudinal chains that compose the ribbon structure; $2N_z$ is the total number of independent sites in the positions $\mathbf{d}_j$ $(j=1,\ldots,2N_z)$ within the primitive cell of length a in the x direction and width W in the transverse direction. The average width of a ribbon with N_z zigzag carbon chains is

$$W = \frac{b}{2}(N_z - 1), \quad b = a\sqrt{3} = 4.26\ \text{Å}. \quad (9)$$

A typical width $W=100$ nm corresponds to $N_z=470$; this is also the rank of the matrices entering recursive step of the decimation-renormalization procedures we handle for the description of the transport properties of graphene ribbons.[23,32]

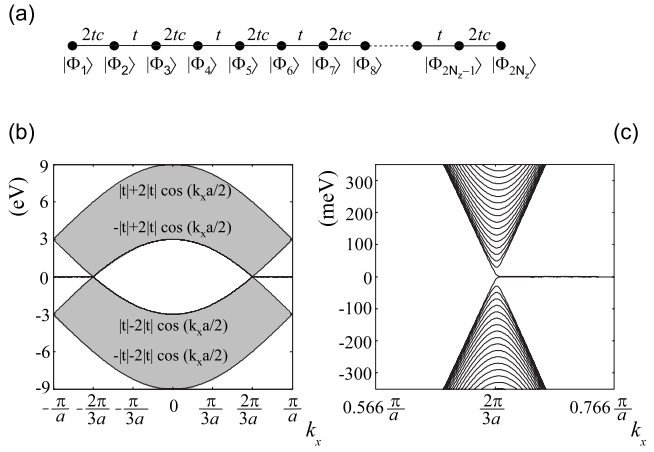

FIG. 3. (a) One-chain model Hamiltonian for the calculation of the energy bands of the graphene wire in the absence of magnetic fields; $\Phi_i(k_x,\mathbf{r})$ $(i=1,2,3,\ldots,2N_z)$ denote the Bloch sums and $c(k_x)=\cos(k_x a/2)$ with $-\pi/a \leqslant k_x < +\pi/a$. (b) Quasicontinuum allowed energy bands of a graphene ribbon of width $W=100$ nm and $N_z=470$, delimited by the four curves $E(k_x)=\mp t \mp 2t\cos(k_x a/2)$. The dispersionless edge states are also indicated. (c) Magnification of the band structure around $E=0$ at the K Dirac point.

The energy bands of graphene ribbons of arbitrary length $L=N_x a$ are obtained by considering the $2N_z$ Bloch sums,

$$\Phi_i(k_x,\mathbf{r}) = \frac{1}{\sqrt{N_x}}\sum_{\mathbf{t}_m} e^{i\mathbf{k}\cdot(\mathbf{t}_m+\mathbf{d}_i)}\phi_{p_z}(\mathbf{r}-\mathbf{d}_i-\mathbf{t}_m),$$

$$i=1,2,\ldots,2N_z, \quad (10)$$

where $\mathbf{k}=(k_x,0)$, $\mathbf{t}_m=(ma,0)$, and the Brillouin zone extends in the range $-\pi/a \leqslant k_x < +\pi/a$. We first study the energy bands in the absence of external magnetic fields and then generalize the treatment to the presence of magnetic fields.

The diagonal elements of the Hamiltonian on the basis (10) are all zero in the nearest neighbor interaction approximation. Off-diagonal matrix elements are different from zero only between adjacent Bloch functions. In summary, on the basis functions $\{\Phi_i(k_x,\mathbf{r})\}$, the Hamiltonian of a zigzag ribbon, in the case $B=0$, assumes the tridiagonal form,

$$H(k_x) = \begin{pmatrix} 0 & 2tc & 0 & 0 & 0 & \ldots \\ 2tc & 0 & t & 0 & 0 & \ldots \\ 0 & t & 0 & 2tc & 0 & \ldots \\ 0 & 0 & 2tc & 0 & t & \ldots \\ 0 & 0 & 0 & t & 0 & \ldots \\ \ldots & \ldots & \ldots & \ldots & \ldots & \ldots \end{pmatrix}_{2N_z} \quad c(k_x) = \cos\frac{k_x a}{2}. \quad (11)$$

For fixed k_x value, the system described by the Hamiltonian (11) is equivalent to the model chain Hamiltonian of Fig. 3(a). The numerical calculations of the band structure of graphene ribbons with $N_z=470$ are reported in Fig. 3(b). The

typical conical structure at the Dirac points near the reference energy $E=0$ is reported in Fig. 3(c).

A close inspection of Fig. 3(b) shows the following features: (i) symmetry of the electronic structure for positive and negative energy values, (ii) strong degeneracy of the energy bands of the ribbon at the points $k_x=\pm\pi/a$, and (iii) occurrence of two partially dispersionless energy bands at $E=0$ (over one-third of the Brillouin zone). For what concerns Fig. 3(c), it is apparent that the energy bands are reminiscent of the Dirac conical shape, broken into discretized electron and hole minibands due to the finite width of the wire. We now analyze the above features of the electronic structure of graphene ribbons analytically.

At the border of the Brillouin zone, for $k_x=\pm\pi/a$, the quantity $\cos(k_x a/2)$ vanishes. From the Hamiltonian (11) or its graphical representation of Fig. 3(a) we have for the energy spectrum

$$E=0 \quad \text{(twofold degenerate)},$$

$$E=+|t|;-|t| \ (N_z-1\text{-fold degenerate each}).$$

This justifies the behavior and the collapse of the energy bands of the zigzag wires at the borders of the Brillouin zone. Other general features of the zigzag ribbon energy bands reported in Figs. 3(b) and 3(c) can be understood with the explicit analytic calculation of the Green's functions corresponding to the tridiagonal Hamiltonian (11).

Consider first the Green's function corresponding to the tridiagonal Hamiltonian operator of Fig. 3(a), assumed to be semi-infinite, i.e., in the limit $2N_z\to\infty$ (later we will consider the case of ribbons of finite width). On the surface site of Fig. 3(a), the retarded Green's function $G_{11}^R(E,k_x;N_z\to\infty)$, denoted simply as $G(E,k_x)$ or $G(E)$, is given by the continued fraction,

$$G(E)=\cfrac{1}{E-4t^2c^2\cfrac{1}{E-t^2\cfrac{1}{E-4t^2c^2\cfrac{1}{E-\cdots}}}}$$

$$\equiv\cfrac{1}{E-4t^2c^2\cfrac{1}{E-t^2G(E)}}. \tag{12}$$

It follows

$$G=\frac{E-t^2G}{E^2-t^2EG-4t^2c^2},$$

from which

$$-t^2EG^2+(E^2-4t^2c^2+t^2)G-E=0.$$

The ribbon Green's function projected onto the orbital at the origin of the semi-infinite chain takes the expression

$$G(E,k_x)=\frac{E^2-4t^2c^2+t^2\mp\sqrt{(E^2-4t^2c^2+t^2)^2-4t^2E^2}}{2t^2E}. \tag{13}$$

The sign in front of the square root must be chosen in such a way that it conserves the Herglotz property of the retarded Green's function: (i) In the energy regions where the discriminant $D(E,k_x)<0$, the Green's function is complex, and the sign of the square root must be chosen so that the imaginary part of the retarded Green's function is negative. (ii) In the energy regions where $D(E,k_x)>0$, the Green's function is real, and the sign in front of the square root must be chosen so that the energy derivative of the Green's function is negative.

The discriminant of the quadratic equation is

$$\begin{aligned}D(E,k_x)&=(E^2-4t^2c^2+t^2)^2-4t^2E^2\\&=(E-t-2tc)(E-t+2tc)\\&\quad\times(E+t-2tc)(E+t+2tc).\end{aligned} \tag{14}$$

In the last line, the discriminant has been conveniently written as the product of four factors. The zero values of $D(E,k_x)$ in the (E,k_x) space define four curves, which separate the energy region where the Green's function has an imaginary part, from those where it is real and no state is possible. The delimiting curves have the expressions

$$E(k_x)=\mp t\mp 2t\cos\frac{k_x a}{2}, \tag{15}$$

and are reported in Fig. 3(b); the allowed energy regions, delimited by the four curves, are shadowed.

The continued fraction elaboration in the context of Bloch functions of k_x wave number, here adopted, constitutes an elegant complement to the efficient real space treatments of electronic states[5,39–41] and Green's functions[42,43] in graphitic ribbons. In fact, inspection of the continued fraction [Eq. (12)], and its exact resummation [Eq. (13)], permits to describe and to discern naturally also the edge states at zero energy, characterizing the bipartite zigzag wires. From Eq. (13), we can easily identify the presence of surface (edge) states at energy $E=0$. The Green's function in the energy shell around $E=0$ following prescription (ii) becomes

$$G(E,k_x)=\frac{E^2-4t^2c^2+t^2+\sqrt{(E^2-4t^2c^2+t^2)^2-4t^2E^2}}{2t^2E}.$$

For $E\to 0+i\epsilon$ (ϵ positive infinitesimal quantity), the Green's function takes the form

$$G(E,k_x)=\begin{cases}\dfrac{1-4c^2}{E} & \text{if } 0\leqslant c(k_x)<\dfrac{1}{2}\\[2ex]\dfrac{E}{(1-4c^2)t^2} & \text{if } \dfrac{1}{2}<c(k_x)\leqslant 1.\end{cases}$$

From the above equation, it is seen that zero energy edge states occur in the Brillouin zone if $0\leqslant\cos(k_x a/2)<1/2$, i.e., for $-\pi/1\leqslant k_x<-(2/3)\pi/a$ and $+(2/3)\pi/a<k_x\leqslant\pi/a$, and the weight of each pole is $1-4c^2$.

We pass now to consider the analytic determination of the energy levels at the Dirac points in zigzag graphene ribbons. The matrix Hamiltonian (11) for $k_x=(2/3)(2\pi/a)$ describes a chain with $2N_z$ sites and constant interaction t between nearest neighbors. The $2N_z$ eigenvalues of the finite chain are given by the expression[44]

$$E_n = 2t\cos\frac{n}{2N_z+1}, \quad \pi n = 1,2,\ldots,2N_z. \tag{16a}$$

We are interested in the energy values around the zero reference energy of the Dirac points. To explore this region for sufficiently large N_z, we set $n=N_z-m$, where m is an integer number, and exploit the identity

$$\frac{N_z-m}{2N_z+1}\pi = \frac{\pi}{2} - \left(m+\frac{1}{2}\right)\frac{1}{2N_z+1}\pi.$$

Equation (16a) can thus be written as

$$E_m = 2t\sin\left[\left(m+\frac{1}{2}\right)\frac{\pi}{2N_z+1}\right], \quad -N_z \leqslant m < +N_z. \tag{16b}$$

The eigenvalues of the finite chain, near the reference energy, are given (with very good approximation for large N_z and $|m| \ll N_z$) by the expression

$$E_m \approx \left(m+\frac{1}{2}\right)|t|\frac{\pi}{N_z+1/2},$$

$$m = 0, \mp 1, \mp 2, \ldots \quad (|m| \ll N_z). \tag{17}$$

Notice that the results of Eqs. (16a), (16b), and (17) depend only on $|t|$ and N_z and are independent of the lattice parameter.

The energy levels [Eq. (17)] constitute a ladder with rungs separated by

$$\Delta = |t|\frac{\pi}{N_z+1/2}. \tag{18}$$

The rungs nearest the reference energy $E=0$ are at energies $\pm\Delta/2$ (corresponding to $m=0$ and $m=-1$). From this result and Fig. 3(c), it is seen that a single electron conductive channel is active for positive Fermi energies of the injected electrons up to $3\Delta/2$, and then two more conductive channels (one per valley) become active at each increase Δ of the Fermi energy. By virtue of the electron-hole symmetry of the energy spectrum, similar properties hold for holelike carriers at negative energies.

We can recast Eq. (17) in the equivalent form

$$E_m = \frac{\sqrt{3}}{2}|t|a\left(m+\frac{1}{2}\right)\frac{\pi}{W_{\text{cont}}} \quad \text{with } W_{\text{cont}} = \frac{b}{2}\left(N_z+\frac{1}{2}\right),$$

where W_{cont} ($\approx W$) can be considered as the width of the ribbons with N_z chains in the continuum approximation. In fact, in the spirit of the continuum limit and quantization of transverse wave vectors, we write the above expression in the form

$$E_m = \mp\frac{\sqrt{3}}{2}|t|k_y a \quad \text{with } k_y = \left(m+\frac{1}{2}\right)\frac{\pi}{W_{\text{cont}}},$$

$$m = 0,1,2,\ldots .$$

The fact that semi-integer values replace integer values in the quantization rule can be justified by appropriate elaborations of the boundary conditions in the continuum approximation of the honeycomb topology and zigzag longitudinal modulation,[22] while it is automatically handled in the present atomistic description.

We consider now the effect of magnetic fields on the electronic structure of zigzag graphene ribbons. In the tight-binding framework, the magnetic field is described by appropriate Peierls phase factors in the hopping interactions. In the hexagonal lattice of graphene, the magnetic flux through a hexagonal plaquette is

$$\Phi_p(B) = Ba\frac{b}{2} = \frac{\sqrt{3}}{2}a^2B.$$

The corresponding Peierls phase is

$$\alpha = 2\pi\frac{\Phi_p(B)}{\Phi_0} = 2\pi\frac{\sqrt{3}}{2}\frac{a^2B}{\Phi_0} = \frac{\sqrt{3}}{2}\frac{a^2}{l_0^2},$$

where $\Phi_0=\frac{hc}{e}$ and $\alpha\approx 0.79\times 10^{-3}$ for $B=10$ T. The modification of the hopping parameters of the Hamiltonian of graphene, in the presence of magnetic fields, is shown schematically in Fig. 2. In the zigzag graphene ribbon, it is convenient to share the Peierls phase between two adjacent bonds by assigning the phase $\alpha/2$ to each of them.

The Hamiltonian of the system in Fig. 2 is translationally invariant along the longitudinal x direction. Using the basis of the Bloch sums [Eq. (10)] and the matrix elements of the Hamiltonian with the appropriate phase factors in the hopping parameters, we obtain for a ribbon with N_z zigzag chains,

$$H(k_x,B) = \begin{pmatrix} 0 & 2tc_1 & 0 & 0 & 0 & 0 & \ldots \\ 2tc_1 & 0 & t & 0 & 0 & 0 & \ldots \\ 0 & t & 0 & 2tc_2 & 0 & 0 & \ldots \\ 0 & 0 & 2tc_2 & 0 & t & 0 & \ldots \\ 0 & 0 & 0 & t & 0 & 2tc_3 & \ldots \\ 0 & 0 & 0 & 0 & 2tc_3 & 0 & \ldots \\ \ldots & \ldots & \ldots & \ldots & \ldots & \ldots & \ldots \end{pmatrix}_{2N_z}. \tag{19}$$

with $c_n=\cos\left(\frac{k_x a}{2}-\frac{n\alpha}{2}\right)$, $n=1,2,\ldots N_z$. Equation (19) is the generalization of Eq. (11) in the presence of magnetic fields.

We wish to point out an important feature of the tridiagonal Hamiltonian (19). The magnetic band structure given by Eq. (19) is clearly invariant if the arguments of all c_n are modified by a same arbitrary phase. We can use this arbitrariness to require that $E_n(k_x,B)=E_n(-k_x,B)$. For this purpose, we must choose

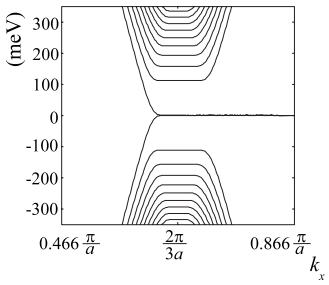

FIG. 4. Allowed magnetic energy bands around the $E=0$ reference energy of graphene ribbons of width 100 nm in a magnetic field of 10 T at the K Dirac point.

$$c_n = \cos\left[\frac{k_x a}{2} - n\frac{\alpha}{2} + Q\frac{\alpha}{2}\right] \quad \text{with } Q = \frac{N_z+1}{2}$$
$$\text{and } n = 1,2,\ldots,N_z. \tag{20}$$

Notice that Q is an integer number if N_z is odd, while it is semi-integer if N_z is even. It follows that

$$c_n(+k_x,\alpha,Q) \equiv c_{N_z+1-n}(-k_x,\alpha,Q) \quad \text{for any } n = 1,2,\ldots,N_z,$$

and thus the values of the energy spectrum at $+k_x$ and $-k_x$ coincide. The magnetic energy bands reported in Fig. 4 are obtained by diagonalization of the matrix [Eq. (19)] with $N_z=470$ for a magnetic field $B=10$ T and the choice [Eq. (20)] for the off-diagonal matrix elements. In this figure, the values of the energies at the Dirac points are well represented by the analytic expression $E_n = \pm\gamma\sqrt{n}$ of Eq. (8).

IV. SPATIAL DISTRIBUTION OF SPECTRAL CURRENTS IN ZIGZAG GRAPHENE RIBBONS

The Keldysh nonequilibrium Green's function method, in combination with the tight-binding representation of the electronic system, provides a powerful tool for the investigation of quantum transport in mesoscopic devices.[28–36] This is due from one side to the general theoretical foundations of the method, directly based on the many-body formalism, and from the other side to its flexibility in obtaining accurate numerical solutions of the kinetic transport equations at the atomistic level also exploiting the renormalization-decimation method or other recursive techniques. The formal expressions of current profiles and the numerical recipes for their actual evaluation have been thoroughly discussed in papers[31,32] for the standard case of electron carriers on square lattices. Along similar guidelines, an appropriate procedure has been implemented for the calculation of current profiles in the honeycomb topology, where carriers can have either electronlike or holelike nature.

In the simulation of quantum transport in the presence of magnetic fields (unitary class systems) or also in the presence of spin-orbit interactions (simplectic class systems), it is essential to discern background (or persistent) local currents, whose total net value through any section of the device is vanishing, from transport local currents, whose total net value through any section of the device is constant and represents the measured current flowing from lead to lead. This problem has been discussed quantitatively in Ref. 32 in order to achieve optimized quantum simulations, and we refer to it for procedures and technical details. Throughout this paper, we only focus on transport currents and their spatial distribution.

The purpose of this section is the computation of transport current profiles through zigzag nanoribbons of graphene in the absence or in the presence of uniform magnetic fields and gate potentials. Ideal left and right leads connect the system to two particle reservoirs at the chemical potentials μ_L and μ_R, respectively. In the simulations, we assume $\mu_L < \mu_R$, so that carriers are injected from the right lead to the left one. In the linear response regime, we also assume $\mu_L \approx \mu_R$, with $\mu_L = E_F - \epsilon$ and $\mu_R = E_F + \epsilon$, where $\epsilon \to 0^+$. For brevity, we denote with E (or E_F) the energy of the injected carriers.

We start describing current distributions through n-type or p-type zigzag graphene ribbons in the absence of magnetic fields. In the simulations, we have chosen nanoribbons of width $W=100$ nm and Fermi energy $E_F=+150$ meV; the energy band structure of the system has been discussed previously and shown in Fig. 3(c). The structure is translationally invariant in the longitudinal x direction and the current flow is determined by the N active channels intersected by the Fermi energy ($N=15$ in the chosen specific example; a multichannel simulation has been chosen because it is less sensitive to geometrical parameters than a single channel situation with possible filter effects). The microscopic current profile is reported in Fig. 5(a). The current flows mainly in the bulk of the device, and its transverse profile is related to the nodal structure of the wave functions in the conductive channels intersected by the Fermi energy. The current profile does not change if the Fermi energy is shifted from +150 meV to the symmetric value of −150 meV. We have also verified that the conductance is exactly given by $G = 15 \times (2e^2/h)$. The conductance quantization is related to the translational symmetry of the ribbon in the longitudinal direction. In orthogonal class systems (e.g., in the absence of magnetic fields), this quantization is fragile with respect to any source of disruption of the translational symmetry.

We consider now the same unipolar ribbon subjected to a uniform magnetic field $B=10$ T, perpendicular to the carbon sheet. The magnetic energy bands of the nanoribbon are reported in Fig. 4. Three conductive channels are active at $E_F=150$ meV. The current distribution, reported in Fig. 5(b), is confined to the lower edge of the ribbon and involves a region of width of the order of the magnetic length ($l_0 \approx 80$ Å for $B=10$ T). Intuitively, this occurs by virtue of the Lorentz force acting on the electron carriers injected from the right lead and moving toward the left lead. The Hall conductance of the device is quantized with value $G=3 \times (2e^2/h)$. Notice that in the unitary class systems (e.g., in the presence of magnetic fields), when the magnetic length is much lower than the width of the sample, the quantization of the Hall conductance is robust with respect to possible sources of disruption of the longitudinal translational symmetry because of the quenching of backscattering processes.

In Fig. 5(c), we report the current distribution in the same structure, when the Fermi energy is displaced from the value $E_F=+150$ meV to the symmetric value of −150 meV and $B=10$ T. The current distribution is now confined to the up-

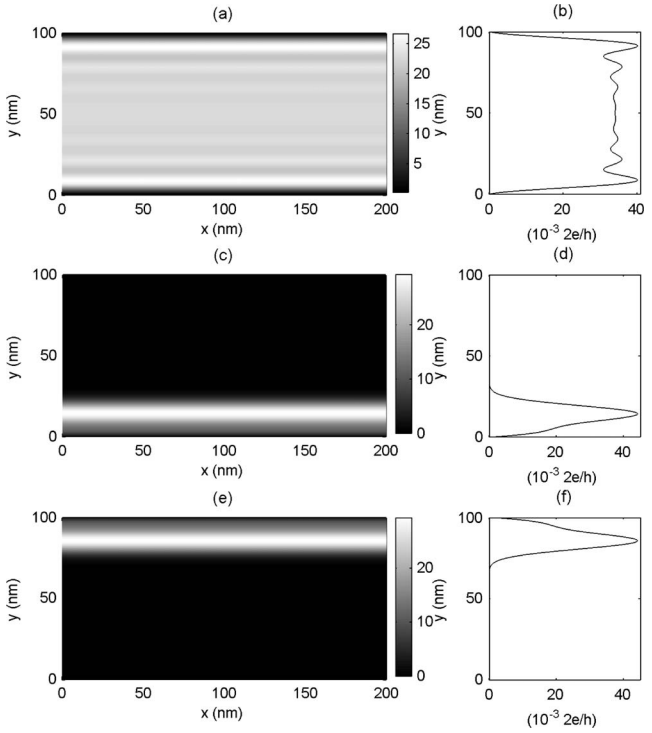

FIG. 5. (a) Spatial distribution of spectral current for a zigzag graphene ribbon of width $W=100$ nm and Fermi energy $E_F = \pm 150$ meV; conductance is $G=15\times 2e^2/h$. (b) Spatial distribution of spectral current at energy $E_F=+150$ meV for the same graphene ribbon in the presence of uniform magnetic field of value $B=10$ T. The current flows only in the lower edge of the sample, and the conductance is $G=3\times 2e^2/h$. (c) Spatial distribution of spectral current at energy $E_F=-150$ meV for the same graphene ribbon in the presence of uniform magnetic field of value $B=10$ T. The current flows only in the upper edge of the sample, and the conductance is $G=3\times 2e^2/h$. In the right panels, the corresponding transverse profiles of the microscopic currents are reported. The unit of the spectral current in the grey scale is $i_0=2e/h$. No external gate potential is applied.

per edge of the ribbon by virtue of the Lorentz force acting on the holelike carriers of the structure.

The message from Fig. 5 can be summarized as follows: In the absence of magnetic fields, the current flows mainly in the bulk of the ribbon, and there is no difference in the spectral current distribution if the Fermi energy lies at $+E_F$ (electronlike carriers) or $-E_F$ (holelike carriers). On the contrary, in the presence of strong magnetic fields, quantized chiral currents occur at opposite edges of the ribbon, and manipulation of currents becomes possible by acting on the electron or hole nature of carriers, with p or n doping of the material.

The manipulation of currents by shifting the Fermi energy of the charge carriers, although of interest, does not appear as the most convenient way to exploit the electron-hole nature of the Dirac particles. An appealing alternative procedure exploits the application of top gate voltages to create puddles of holes (or electrons) in appropriate regions of the device.

In Fig. 6, we show current profiles through the nanoribbon with a superimposed electrostatic energy V in the region at the left of the transverse section at the origin of the x axis.

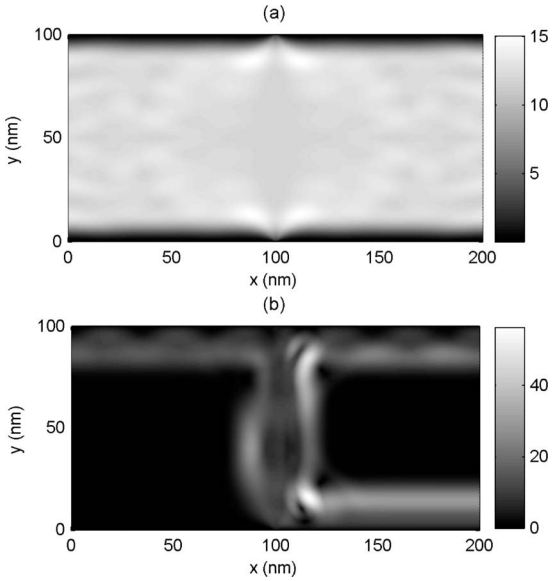

FIG. 6. Current profiles through a graphene ribbon of width 100 nm, with a steplike electrostatic potential gate of value $V=300$ meV in the region $x<100$ nm. (a) Spatial distribution of spectral current at the energy $E_F=150$ meV in the gated graphene ribbon in the absence of magnetic fields. (b) Spatial distribution of spectral current at the energy $E_F=150$ meV in the same gated graphene ribbon in the presence of the magnetic field $B=10$ T. The unit of spectral current is $i_0=2e/h\times 10^{-3}$.

Figure 6(a) shows the distribution of currents when carriers are injected at energy $E_F=150$ meV in the presence of a potential step $V=2\times E_F=300$ meV and in the absence of magnetic fields. From the current distribution reported in Fig. 6(a), it is seen that the current flows mainly in the bulk of the system and is somewhat squeezed in the gated region. The total conductance $G=14.5\times(2e^2/h)$ is near to the value of 15 of the unipolar device of Fig. 5(a) and denotes an efficient Klein tunneling of Dirac particles through the step barrier. In the presence of the gate potential and of a uniform magnetic field of 10 T, the current profiles is shown in Fig. 6(b). The carriers behave as electrons in the right region of the device, and as holes in the left part. Thus, the injected current is expected to flow in the lower edge in the right part and in the upper edge in the left part of the structure. The injected spectral current is perfectly quantized to $3\times(2e^2/h)$; the conductance of the ribbon is about $2\times(2e^2/h)$. Around the junction, the carriers cross the device from edge to edge, invading the bulk of the sample. Note that the bulk of the sample in the presence of magnetic fields is strictly prohibited to the carrier flow [as illustrated in Figs. 5(b) and 5(c), and also in Fig. 6(c) in the regions far enough from the junction].

In Fig. 7, we consider current profiles through a n-p-n structure, obtained with a superimposed electrostatic voltage $V=300$ meV confined in the barrier region extending for 100 nm between the indicated transverse sections. The situations of Figs. 7 and 6 are different for the fact that the semi-infinite steplike barrier is now replaced by a finite rectangular barrier; in the simulations, the p-doped region is a square of edge 100 nm.

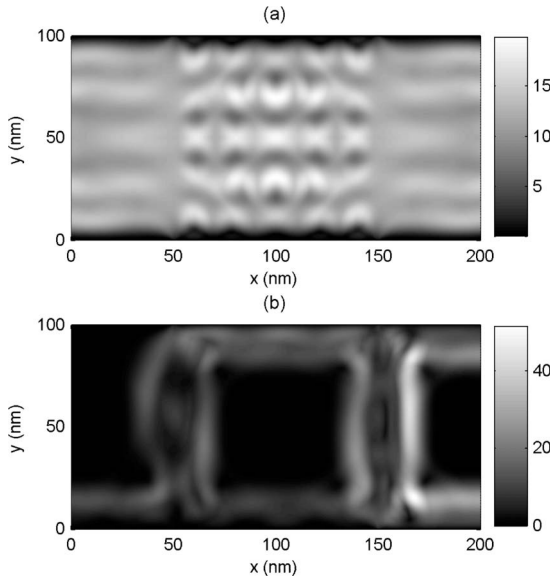

FIG. 7. Current profiles through a graphene ribbon of width 100 nm, with a superimposed electrostatic potential gate of value $V=300$ meV in the region $50<x<150$ nm. (a) Spatial distribution of spectral current at the energy $E_F=150$ meV in the gated graphene ribbon in the absence of magnetic fields. (b) Spatial distribution of spectral current at the energy $E_F=150$ meV in the same gated graphene ribbon in the presence of the magnetic field $B=10$ T. The unit of spectral current is $i_0=2e/h\times 10^{-3}$.

From the current distribution of Fig. 7(a), we see that the current in the *n-p-n* device flows in the bulk of the system, with a total conductance $G\approx 14.5\times(2e^2/h)$ close to the value of unipolar *n*-type device and to the value of the *p-n* junction. Again, this denotes the efficient Klein tunneling of Dirac particles through the rectangular barrier. Notice that differently from Figs. 5(a) and 6(a), the current maps of Fig. 7(a) show a rich pattern related to the back-and-forth scattering of carriers in the gated region.

In the presence of a uniform magnetic field of 10 T and of the same square barrier of 300 meV, the current profile at the injection energy $E_F=150$ meV is shown in Fig. 7(b). The carriers behave as electrons in the right and left regions of the device and as holes in the central part. Thus, the current is expected to flow along the lower edge in the left and right leads and along the upper edge in the central part. The current invades the bulk of the sample and transits from the lower edge to the upper edge at the entrance of the *p* region and turns back to the lower edge on the exit. The main message of Figs. 6 and 7 is the possibility of manipulating current flow of relativistic particles with top gate potentials. This may envisage the possibility of multiterminal carbon devices for quantum logic gates, implementing concepts and geometries of conventional coupled quantum wires[45] or magnetically switched waveguide qubits.[46]

V. CONCLUSIONS

We studied the electronic structure and current profiles in zigzag graphene ribbons within the tight-binding framework and the nonequilibrium Keldsyh Green's function method for quantum transport. Simulations of charge transport in unipolar and bipolar devices, also in the presence of magnetic fields, have been investigated numerically. Insights of the computed results have been provided by the analytic treatment of the electronic structure and conductive channels of relativisticlike particles.

We have shown that in *n-p-n* devices, realized when the height of the gate potential barrier is larger than the energy of the injected carriers, electron particles turn into holes inside the barrier and turn back to electrons outside it. Imaging of current profiles here presented gives a vivid picture of the easy Klein tunneling through barriers by virtue of the electronlike or holelike behavior of the relativistic particles in the *n*-doped and *p*-doped regions. The current maps are of particular interest in the presence of magnetic fields since the spatial distribution of currents is sensitive to the nature of the carriers. In strong magnetic fields, electrons and holes flow along opposite edges of the sample and we have shown that current manipulation is in principle possible by means of top gates.

The investigations of this paper concern the current distribution of relativistic particles in two-terminal devices under rectangular steplike superimposed gate potentials; a wealth of other situations could be envisaged along similar guidelines. It is likely that appropriate geometries of top gates or multiterminal devices offer further flexibility in manipulation of currents, focusing of electron beams, realization of ideal or nearly ideal electronic lenses, and design of novel devices based on charge conjugation symmetry of Dirac particles.

ACKNOWLEDGMENTS

This work has been supported by Scuola Normale Superiore and by National Enterprise for Nanoscience and Nanotechnology (NEST).

[1] P. R. Wallace, Phys. Rev. **71**, 622 (1947).
[2] G. Dresselhaus and M. S. Dresselhaus, Phys. Rev. **140**, A401 (1965).
[3] F. Bassani and G. Pastori Parravicini, Nuovo Cimento B **50**, 95 (1967).
[4] E. Doni and G. Pastori Parravicini, Nuovo Cimento B **64**, 117 (1969).
[5] R. Saito, G. Dresselhaus, and M. S. Dresselhaus, *Physical Properties of Carbon Nanotubes* (Imperial College, London, 1998).
[6] B. Partoens and F. M. Peeters, Phys. Rev. B **74**, 075404 (2006); **75**, 193402 (2007).
[7] J.-C. Charlier, X. Blase, and S. Roche, Rev. Mod. Phys. **79**, 677

(2007).
[8] G. Grosso and G. Pastori Parravicini, *Solid State Physics* (Academic, London, 2000).
[9] G. W. Semenoff, Phys. Rev. Lett. **53**, 2449 (1984).
[10] K. S. Novoselov, A. K. Geim, S. V. Morozov, D. Jiang, Y. Zhang, S. V. Dubonos, I. V. Grigorieva, and A. A. Firsov, Science **306**, 666 (2004).
[11] K. S. Novoselov, A. K. Geim, S. V. Morozov, D. Jiang, M. I. Katsnelson, I. V. Grigorieva, S. V. Dubonos, and A. A. Firsov, Nature (London) **438**, 197 (2005).
[12] Y. Zhang, Y.-W. Tan, H. L. Stormer, and P. Kim, Nature (London) **438**, 201 (2005).
[13] C. Berger, Z. Song, X. Li, X. Wu, N. Brown, C. Naud, D. Mayou, T. Li, J. Hass, A. N. Marchenkov, E. H. Conrad, P. N. First, and W. A. de Heer, Science **312**, 1191 (2006).
[14] J. R. Williams, L. DiCarlo, and C. M. Marcus, Science **317**, 638 (2007).
[15] A. Abanin and L. S. Levitov, Science **317**, 641 (2007).
[16] B. Huard, J. A. Sulpizio, N. Stander, K. Todd, B. Yang, and D. Goldhaber-Gordon, Phys. Rev. Lett. **98**, 236803 (2007).
[17] B. Özyilmaz, P. Jarillo-Herrero, D. Efetov, D. A. Abanin, L. S. Levitov, and P. Kim, Phys. Rev. Lett. **99**, 166804 (2007).
[18] J. Cserti, Phys. Rev. B **75**, 033405 (2007).
[19] K. Ziegler, Phys. Rev. B **75**, 233407 (2007).
[20] N. M. R. Peres, F. Guinea, and A. H. Castro Neto, Phys. Rev. B **73**, 125411 (2006).
[21] N. M. R. Peres, A. H. Castro Neto, and F. Guinea, Phys. Rev. B **73**, 195411 (2006).
[22] J. Tworzydlo, B. Trauzettel, M. Titov, A. Rycerz, and C. W. J. Beenakker, Phys. Rev. Lett. **96**, 246802 (2006).
[23] A. Cresti, G. Grosso, and G. P. Parravicini, Phys. Rev. B **76**, 205433 (2007).
[24] M. I. Katsnelson, K. S. Novoselov, and A. K. Geim, Nat. Mater. **2**, 620 (2006).
[25] M. I. Katsnelson, Eur. Phys. J. B **51**, 157 (2006).
[26] J. B. Pendry, Science **315**, 1226 (2007).
[27] V. V. Cheianov, V. Fal'ko, and B. L. Altshuler, Science **315**, 1252 (2007).
[28] D. K. Ferry and S. M. Goodnick, *Transport in Nanostructures* (Cambridge University Press, Cambridge, 1997).
[29] R. Lake, G. Klimeck, R. Brown, and D. Jovanovich, J. Appl. Phys. **81**, 7845 (1997).
[30] S. Datta, *Electronic Transport in Mesoscopic Systems* (Cambridge University Press, Cambridge, 1995).
[31] A. Cresti, R. Farchioni, G. Grosso, and G. P. Parravicini, Phys. Rev. B **68**, 075306 (2003).
[32] A. Cresti, G. Grosso, and G. Pastori Parravicini, Eur. Phys. J. B **53**, 537 (2006).
[33] M. Mendoza and P. A. Schulz, Phys. Rev. B **71**, 245303 (2005).
[34] G. Metalidis and P. Bruno, Phys. Rev. B **72**, 235304 (2005).
[35] F. Triozon and S. Roche, Eur. Phys. J. B **46**, 427 (2005).
[36] B. K. Nikolić, L. P. Zârbo, and S. Souma, Phys. Rev. B **73** 075303 (2006).
[37] L. P. Zârbo and B. K. Nikolić, Europhys. Lett. **80**, 47001 (2007).
[38] C. Töke, P. E. Lammert, V. H. Crespi, and J. K. Jain, Phys. Rev. B **74**, 235417 (2006).
[39] K. Wakabayashi, M. Fujita, H. Ajiki, and M. Sigrist, Phys. Rev. B **59**, 8271 (1999).
[40] K. Nakada, M. Fujita, G. Dresselhaus, and M. S. Dresselhaus, Phys. Rev. B **54**, 17954 (1996).
[41] L. Brey and H. A. Fertig, Phys. Rev. B **73**, 235411 (2006).
[42] Z. F. Wang, R. Xiang, Q. W. Shi, J. Yang, X. Wang, J. G. Hou, and J. Chen, Phys. Rev. B **74**, 125417 (2006).
[43] Z. F. Wang, Q. Li, H. Su, X. Wang, Q. W. Shi, J. Chen, J. Yang, and J. H. Hou, Phys. Rev. B **75**, 085424 (2007).
[44] See, e.g., A. Sutton, *Electronic Structure of Materials* (Clarendon, Oxford, 1993), p. 41.
[45] A. Bertoni, P. Bordone, R. Brunetti, C. Jacoboni, and S. Reggiani, Phys. Rev. Lett. **84**, 5912 (2000).
[46] J. Harris, R. Akis, and D. K. Ferry, Appl. Phys. Lett. **79**, 2214 (2001).